geosciences

MDPI

Article

The Subduction-Related Metavolcanic Rocks of Maroua, Northern Cameroon: New Insights into a Neoproterozoic Continental Arc Along the Northern Margin of the Central African Fold Belt

Pierre Christel Biakan à Nyotok [1], Merlin Gountié Dedzo [2,*], Diddi Hamadjoda Djamilatou [1,3], Nils Lenhardt [3], Moussa Ngarena Klamadji [4], Periclex Martial Fosso Tchunte [1] and Pierre Kamgang [5]

1 Department of Earth Sciences, Faculty of Science, University of Maroua, Maroua P.O. Box 814, Cameroon; biakanpierre@gmail.com (P.C.B.à.N.); diddidjamilatou690@gmail.com (D.H.D.); fossopericlex@yahoo.fr (P.M.F.T.)
2 Department of Life and Earth Sciences, High Teachers' Training College, University of Maroua, Maroua P.O. Box 55, Cameroon
3 Department of Geology, University of Pretoria, Private Bag X20, Pretoria 0028, South Africa; nils.lenhardt@up.ac.za
4 Département des Sciences de la Vie et de la Terre, Faculté des Sciences Techniques et de la Technologie, Université de Pala, Pala P.O. Box 28, Chad; klamadjimoussa@yahoo.fr
5 Department of Earth Sciences, University of Yaoundé I, Yaoundé P.O. Box 812, Cameroon; pkamgan@yahoo.fr
* Correspondence: merlin.gountie@gmail.com

Abstract: The metavolcanic rocks around Maroua in the Far North Region of Cameroon are located at the northern margin of the Central African Fold Belt (CAFB) and have not been studied to date. The petrographic and whole-rock geochemical data presented in this paper highlight their magma genesis and geodynamic evolution. The lavas are characterized by basaltic, andesitic, and dacitic compositions and belong to the calc-alkaline medium-K and low-K tholeiite series. The mafic samples are essentially magnesian, while the felsic samples are ferroan. On a chondrite-normalized REE diagram, mafic and felsic rocks display fractionated patterns, with light REE enrichment and heavy REE depletion (La_N/Yb_N = 1.41–5.38). The felsic samples display a negative Eu anomaly (Eu/Eu* = 0.59–0.87), while the mafic lavas are characterized by a positive Eu anomaly (Eu/Eu* = 1.03–1.35) or an absence thereof. On a primitive mantle-normalized trace element diagram, the majority of the samples exhibit negative Ti and Nb–Ta anomalies (0.08–0.9 and 0.54–0.74, respectively). These characteristic features exhibited by the metavolcanic rocks of Maroua are similar to those of subduction-zone melts. This subduction would have taken place after the convergence between the Congo craton (Adamawa-Yadé domain) and the Saharan craton (Western Cameroonian domain). Petrological modelling using major and trace elements suggests a derivation of the Maroua volcanics from primitive parental melts generated by the 5–10% partial melting of a source containing garnet peridotite, probably generated during the interaction between the subducted continental crust and the lithospheric mantle and evolved chemically through fractional crystallization and assimilation.

Keywords: Central African Fold Belt; Far North Region of Cameroon; metavolcanics of Maroua; subduction-zone melts; fractional crystallization and assimilation

check for updates

Citation: Biakan à Nyotok, P.C.; Gountié Dedzo, M.; Djamilatou, D.H.; Lenhardt, N.; Klamadji, M.N.; Fosso Tchunte, P.M.; Kamgang, P. The Subduction-Related Metavolcanic Rocks of Maroua, Northern Cameroon: New Insights into a Neoproterozoic Continental Arc Along the Northern Margin of the Central African Fold Belt. *Geosciences* **2024**, *14*, 298. https://doi.org/10.3390/geosciences14110298

Academic Editor: Gianluca Groppelli

Received: 15 September 2024
Revised: 26 October 2024
Accepted: 29 October 2024
Published: 5 November 2024

1. Introduction

Despite forming the link between the Precambrian shield of Central Africa and the regions to the north that include the West African Shield and the central Sahara domain, the Central African Fold Belt (CAFB) is the least well-known of all major Pan-African belts [1]. In fact, central Africa, situated north of the Congo basin, is geologically poorly known. Up till now, it holds an essential key to unraveling geologic relations in Africa between the Precambrian shield of central Africa and the areas to the north that comprise the central Sahara domains and the West African Shield. The amalgamation of the Archean and Paleoproterozoic blocks (<1600 Ma) in Central Africa has been carried out in several phases, from the Mesoproterozoic (1600–1000 Ma) to the Neoproterozoic (1000–540 Ma) by the accretion of the various pan-African belts, such as the CAFB. The first phase contributed to the construction of the supercontinent Rodinia, while the second phase helped to build the supercontinent Gondwana [2]. The assembly of this latter continent involved the closure of the intervening Neoproterozoic basins and subduction of the oceanic lithosphere along a convergent margin [3,4]. In the Cameroonian part, especially in the northern part, previous work described the volcano–sedimentary sequence in the Poli, Bibemi-Zalbi, and Rey Bouba Greenstone belts [1,5–7].

The Poli Belt, to which the metavolcanic rocks of Maroua belong, is a syn- to pre-collisional basin established upon or in the environs of young magmatic arcs. The filling up of this depression occurred in a docking-arc/back-arc setting [8]. It comprises Neoproterozoic schists and gneisses of low and medium-to-high grade with sedimentary, volcano–sedimentary and volcanic origin. Metavolcanic rocks are calc-alkaline rhyolite and tholeiitic basalt emplaced in an extensional crustal setting [9,10]. Their depositional age is about 700–665 Ma; detrital sources include ca. 736, 780, 830 and 920 Ma magmatic rocks [8,11].

The Bibemi–Zalbi Belt covers the Cameroonian and Chadian territories and is locally named Bibemi–Zalbi Greenstone Belt. It is dated around 777 ± 5 Ma on epiclastite [12] and 700 ± 10 Ma on metabasalt [13]. According to [14] assumption of a back-arc and an arc basin system associated with a subduction in the Adamawa-Yadé Domain (AYD), [15] interpreted the region in terms of back-arc basin, volcanic arc and fore-arc basin that were accreted eastward to the AYD, alongside the Tchollíré–Banyo shear zone.

The Rey Bouba Greenstone belt (RBGB) principally comprises sedimentary and volcano–sedimentary rocks, felsic volcanic to greenschist-facies mafic rocks associated with pre-, syn- and post-tectonic dykes and granitoids [7]. It is a back-arc basin related to the subduction of an oceanic plate below the southeastern continental margin of the AYD [4,15]. Nevertheless, few geochronological data acquired by Pb–Pb minimum ages on single zircon are available for the RBGB, indicating ages of 750 ± 20 Ma for the Gatougel dacitic tuff [14] and 557± 17 Ma for the post-tectonic Vaimba granite. More recently, U–Pb zircon dating of felsic metavolcanic of RBGB fixed the maximum age for the volcanic activity at ca. 670 Ma [7]. The Balda granite pluton, with U-Pb age of 732.7 ± 7.5 Ma [16], located near the Maroua area, is identified as deformed alkaline granite and formed within a syn-orogenic extensional back-arc basin [16]. These sequences were generally interpreted as pre-tectonic back-arc basins intruded by or associated with the calc-alkaline TTG suite [8,15,16]. However, in the Maroua area, these sequences have been poorly studied, and information concerning their geochemistry and their geodynamic setting is very rare or almost nonexistent.

In this study, to better understand the petrogenesis and geodynamic evolution along the northern margins of the CAFB, petrography and geochemistry of metavolcanic rocks of the Maroua area are presented, and their petrology and tectonic setting are discussed.

2. Regional Geology and Tectonic Setting

The Central African Fold Belt (CAFB), or 'mobile zone' [17,18], is a vast belt area located between the Dahomeyide belt in the west, on the edge of the West African craton, and the Oubanguide belt in the east [19]. It is bounded in the north by the East Saharan metacraton and in the south by the Congo craton (Figure 1a,b). In Cameroon, the CAFB is divided into three geotectonic domains [20–22]. These domains are dominated by various shear zones, one of the most important of which is the Cameroonian Centre Shear Zone (CCSZ) at N70°E [23]. The geotectonic domains include, successively, the following: (1) the Southern Domain, identified as a synthetic basin comprising deposits of less than 625 Ma; (2) the Central Domain, marked by the presence of relics of the Paleoproterozoic basement and which was metamorphosed during the Pan-African orogeny and by the intrusion of batholiths; (3) the Northern Domain, which is considered a back-arc basin that formed between 830 Ma and 665 Ma.

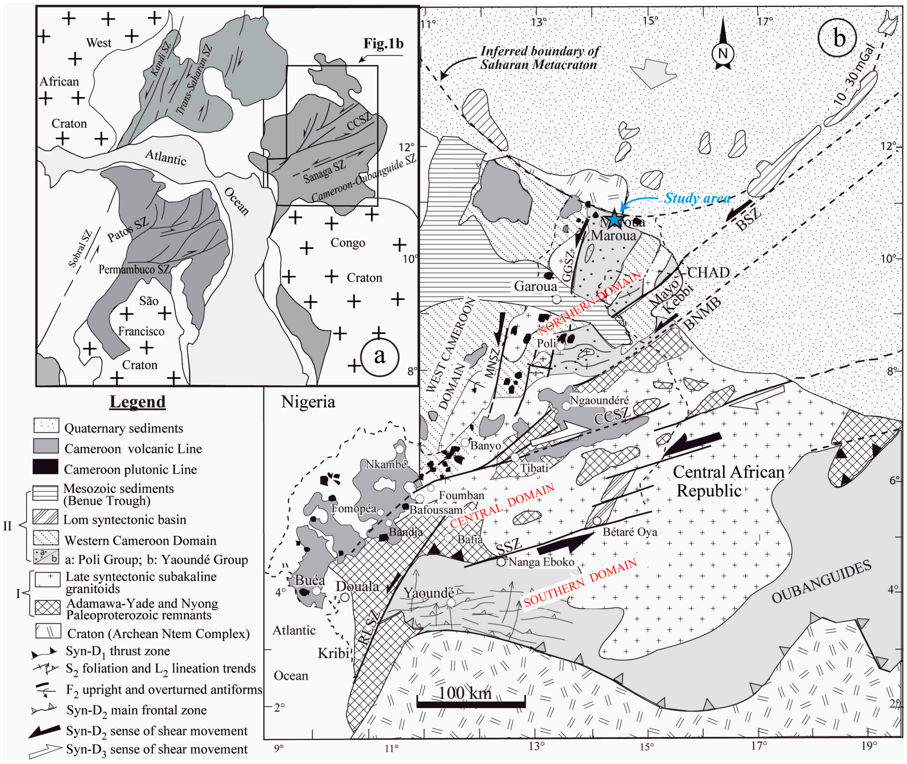

Figure 1. (**a**) Pan-African shear zone network in a pre-Mesozoic reconstruction (modified from [24]); (**b**) Pan-African structural map of Cameroon [23] (modified and reinterpreted from [21]). The inferred boundary of the Saharan metacraton was drawn following [25]. Thick lines indicate shear zones (SZs): BSZ Balché SZ, BNMB Buffle Noir–Mayo Baléo, CCSZ Central Cameroon SZ, GGSZ Godé–Gormaya SZ, MNSZ Mayo Nolti SZ, RLSZ Rocher du Loup SZ, SSZ Sanaga SZ. I, Paleoproterozoic basement and Pan-African syn-tectonic granitoids; II, Meso- to Neoproterozoic volcano–sedimentary basins.

The Southern Domain is bounded to the north by the Sanaga fault and to the south by the northern border of the Congo craton. Three lithological groups are identified in this area: the Yaoundé [26–28], the Mbalmayo [29] and the Ntui–Betamba groups [20]. The area also includes two petrographic units: (1) one unit of metasedimentary rocks (disthene–biotite–garnet gneiss, biotite–muscovite–garnet gneiss, silicate–calcite rocks, and quartzite); (2) one unit of pyroxene and amphibolite–gneiss. These two units recrystallized at temperatures between 750–800 °C and $P \geq 9$–1.3 GPa [20] and correspond to the rocks that were deposited north of the Congo Craton.

The Central or Adamawa-Yadé Domain [7,30] is located between the Buffle Noir–Mayo Baleo (BNMB) fault in the north and the Sanaga fault (FS) in the south [22]. It is characterized by the presence of numerous WSW-ENE Pan-African decay corridors and is composed of several lithological units represented by the following: (i) Paleoproterozoic formations; (ii) Neoproterozoic gneiss; (iii) igneous intrusions of Pan-African age. The Paleoproterozoic formations include plutonic rocks primarily composed of diorites and granodiorites, as well as volcano–sedimentary or metasedimentary rocks such as amphibole and biotite gneisses, garnet and biotite gneisses, meta-arkoses, and meta-quartzites. These formations that are often migmatized, have undergone a remobilization during Pan-African times and have only retained a few relics of granulite assemblages. Geochronological data (U-Pb on zircon) reveal ages for these rocks that are between 2100 Ma and 600 Ma [21,31].

The Northern Domain, or Poli Group [32], to which our study area belongs, is also known as the West Cameroon Domain [7,30]. It is bounded to the west by the Buffle

Noir–Mayo Baleo (BNMB) fault (Figure 1b). This area is considered to be a back-arc basin with an age between 830 and 665 Ma, which is composed of metavolcanic rocks (the object of this study) associated with calc-alkaline tholeiitic bimodal volcanism (tholeiitic basalts, calc-alkaline rhyolites). Furthermore, the Northern Domain includes calc-alkaline intrusions (diorite, granodiorite and granite) that have formed syn- to post-tectonically between 733 and 580 Ma [21,33]. The intrusions penetrated the Paleoproterozoic schists to form NNE–SSW directional batholiths [22]. Furthermore, this domain is characterized by a regional N-S to NNE-SSW foliation.

The Maroua study area (Figure 2) is situated between the latitudes 10°36′40″ N and 10°37′30″ N and the longitudes 14°19′ E and 14°20′ E. It is composed of felsic and mafic metavolcanic lavas, located on the boundary between the Northern Domain and the East Saharan metacraton.

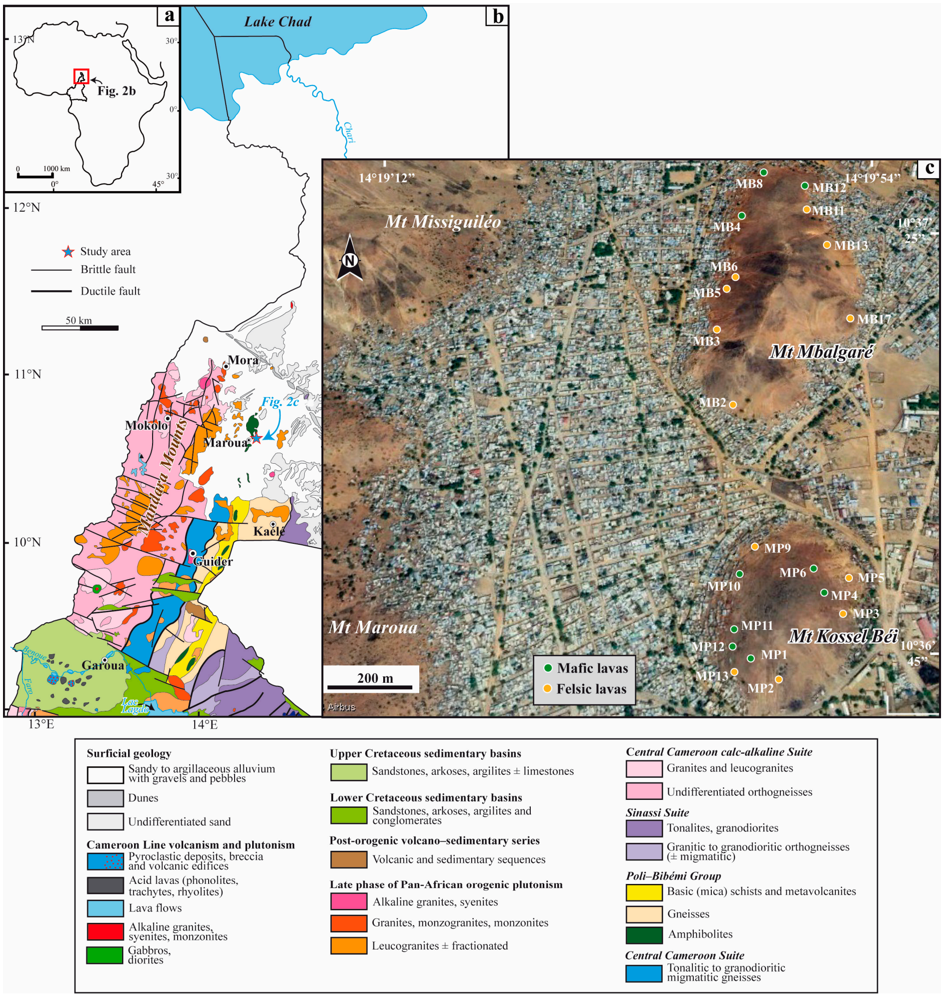

Figure 2. Location of the study area. (**a**) Location of Cameroon in Africa; (**b**) geological map of Northern Cameroon (redrawn from [34]); (**c**) Google map image of the study area with location of the samples for the geochemical analysis.

3. Analytical Methods

For this study, geochemical data of selected samples of the Maroua metavolcanic rocks were obtained. Whole-rock major and trace element concentrations of twenty-one (21) samples were measured by X-ray fluorescence (XRF) and an inductively coupled plasma mass spectrometer (ICP-MS). All samples were finely ground using a tungsten carbide milling pot at the University of Pretoria. For the XRF analyses, major elements and selected trace elements of all samples were analyzed using a Thermo Fischer ARL Perform

X Sequential XRF instrument with OXSAS software (version 2.2). SARM 49 was used for quality control, with accuracy better than 1% for the major element oxides.

At the University of Witwatersrand (WITS), trace element analysis was performed using a Perkin Elmer DRC-e ICP-MS and certified primary solution standards. To ensure the reliability of the data, all the samples were analyzed in conjunction with BCR-1, BHVO-1 and BIR-1 international reference materials. The samples were prepared using the CEM Mars microwave system for HF-HNO_3 digestion and, after drying, were placed in solution with 2% HNO3. For the ICP-MS analysis, the samples were diluted 1000 times and combined with internal Re, Rh, Bi and In standards to provide the needed mass range. Primary external calibration standards were created in the range of 5–100 ppb. Every ICP-MS determination was carried out in the presence of the control standards BCR-1, BHVO-1 and BIR-1. All elements deviated less than 10% from the recommended values.

4. Results

The immobile trace element diagram [35] classified the felsic and mafic volcanic rocks sampled for this investigation as basalts, andesites and dacites (Figure 3a). Almost all mafic samples were chemically classified as subalkaline basalts (Nb/Y = 0.08–0.29) according to the Nb/Y vs. Zr/TiO_2 diagram (Figure 3a). The SiO_2 contents of the mafic rocks (basalt) varied from 49.63 to 60.40 wt% and from 68.00 to 75.25 wt% for the felsic lavas (andesite and dacite). The basalts appeared tholeiitic in composition (Figure 3b), whereas the andesite and dacites appeared calc-alkaline in nature [36] (Figure 3b). Using the SiO_2 vs. K_2O classification diagram of [37], the studied rocks were also found to belong to the calc-alkaline medium-K and low-K tholeiite series (Figure 3c). On the SiO_2 vs. $Fe_2O_3t/(Fe_2O_3t + MgO)$ plot [38], the mafic samples are essentially magnesian, whereas all the felsic rocks are ferroan (Figure 3d).

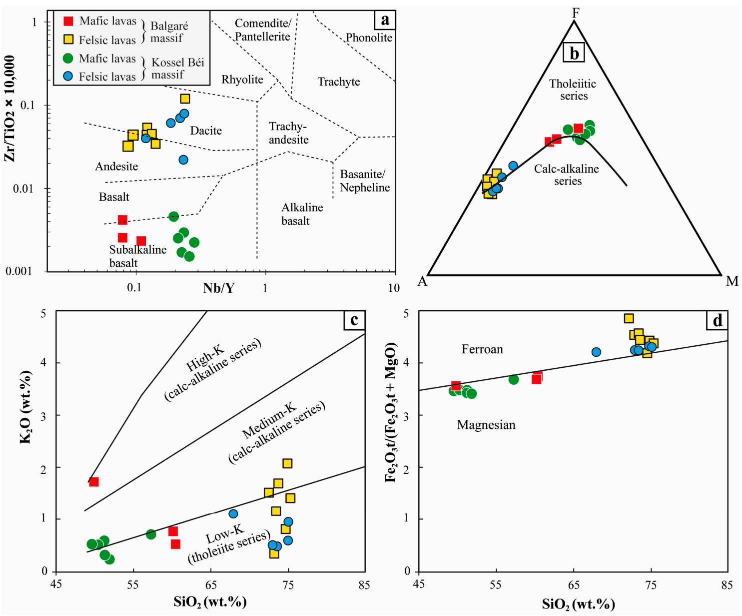

Figure 3. (**a**) Nb/Y versus (vs.) Zr/Ti discrimination diagram plotted for the Maroua felsic and mafic volcanics [35]; (**b**) AFM diagram [36] for the Maroua lavas. Basalts exhibit tholeiitic trends, whereas felsic volcanics are tholeiitic and calc-alkaline in nature. A: $Na_2O + K_2O$; F: FeOt; M: MgO; (**c**) K_2O vs. SiO_2 diagram [37]; (**d**) $[Fe_2O_3t/(Fe_2O_3t + MgO)]$ vs. SiO_2 diagram [38].

The metavolcanic rocks of Maroua are massive and outcrop as blocks and bowls on the slopes of the massifs (Figure 4a,c,e). All samples exhibited microlitic porphyritic and aphyric textures. In the basaltic samples, olivine, clinopyroxene, amphibole, plagioclase and oxides (pyrite was visible in hand specimens of Figure 4b and in thin sections) were the main mineral phases (Figure 5a). The andesites and dacites were found to be mainly composed of quartz (together with feldspar, visible in hand specimens; Figure 4d,f), sanidine, plagioclase, clinopyroxene, biotite and opaque minerals (Figure 5b–d). The matrix of felsic metavolcanic rocks (dacites and andesites) were devitrified and contained abundant, very small crystals of quartz (Figure 5a–c), suggesting that recrystallization had occurred. Fragmented plagioclase, often with flexuous twinning, in mafic and felsic lavas indicated that these rocks were subjected to high pressures after their emplacement.

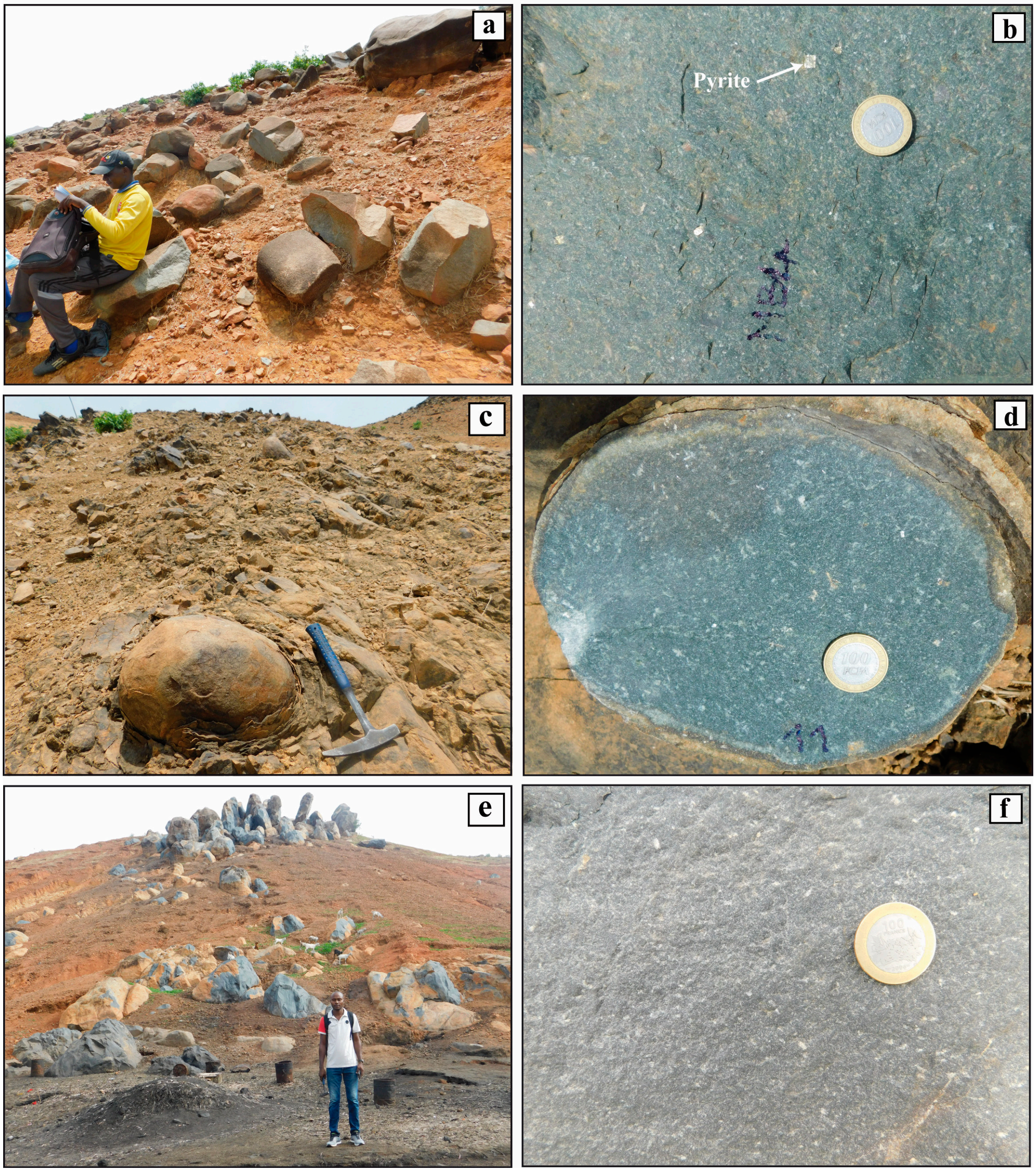

Figure 4. Field outcrop (**a**,**c**,**e**) and hand specimen (**b**,**d**,**f**) photos of the sampled Maroua lavas. (**a**,**b**) Basalt of Mt. Mbalgaré; (**c**,**d**) andesite of Mt. Mbalgaré; (**e**,**f**) dacite of Mt. Kossel Béi.

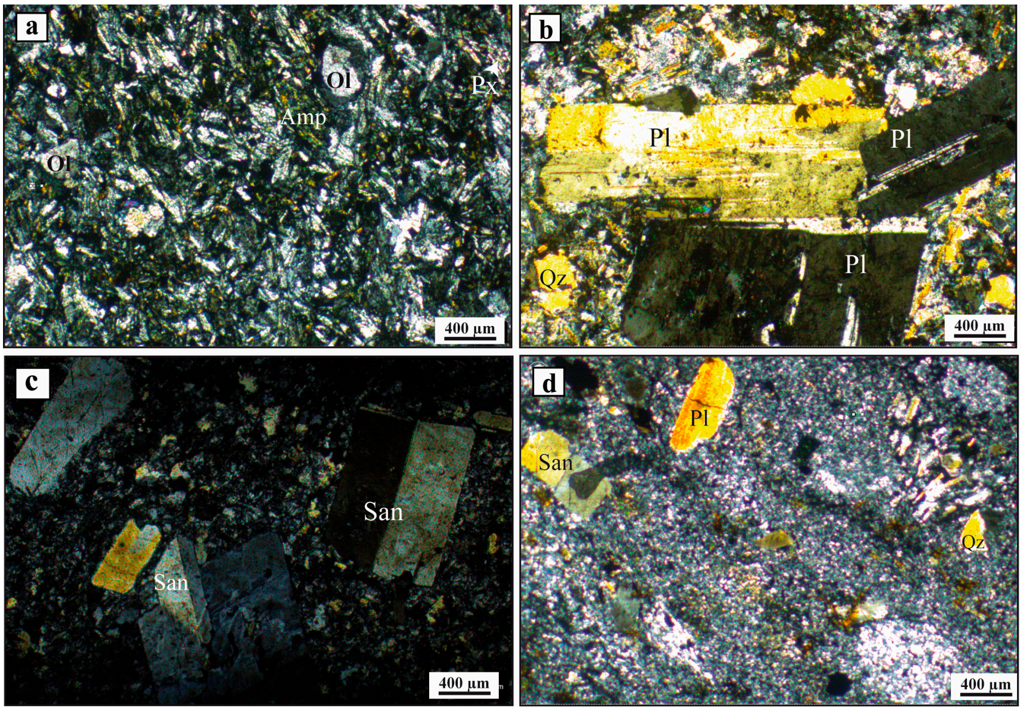

Figure 5. Thin-section photomicrographs of the Maroua lavas. (**a**) Dacite of Mt. Kessel Béi; (**b**) dacite of Mt. Mbalgaré; (**c**) andesite of Mt. Mbalgaré; (**d**) basalt of Mt. Balgaré.

4.1. Geochemistry

Major and trace elements data for representative samples of the Maroua lavas are presented in Tables 1 and 2.

Table 1. Whole-rock major and trace element composition of Maroua volcanic rocks, Mount Kossel Béi.

Rock Type	Basalt	Dacite	Dacite	Basalt	Andesite	Basalt	Andesite	Basalt	Basalt	Basalt	Dacite
Lon. (°E)	14.32929	14.32976	14.33117	14.33074	14.33133	14.33059	14.32931	14.32868	14.32868	14.32868	14.32876
Lat. (°N)	10.61238	10.61216	10.61356	10.61399	10.61435	10.61441	10.61502	10.61400	10.61279	10.61262	10.61221
Sample ID	MP1	MP2	MP3	MP4	MP5	MP6	MP9	MP10	MP11	MP12	MP13
SiO_2 (Wt%)	50.31	75.07	73.12	51.23	73.45	49.63	68.00	51.77	57.22	51.17	74.96
TiO_2	1.09	0.28	0.36	1.22	0.35	1.05	0.50	1.04	0.97	0.96	0.31
Al_2O_3	18.93	14.58	13.40	18.39	13.35	19.19	14.80	18.26	16.97	20.20	13.09
Fe_2O_3	11.11	3.52	4.05	11.07	4.05	11.12	5.81	10.94	10.54	9.77	3.64
MnO	0.17	0.07	0.10	0.22	0.10	0.19	0.15	0.18	0.18	0.18	0.07
MgO	4.89	0.57	0.72	4.99	0.73	4.95	1.08	5.04	3.67	4.47	0.57
CaO	9.92	0.79	1.00	8.32	0.77	10.08	2.74	8.02	5.85	9.47	0.54
Na_2O	2.84	4.42	6.64	3.97	6.64	3.01	5.66	4.25	3.64	2.89	5.77
K_2O	0.50	0.60	0.50	0.33	0.47	0.52	1.11	0.22	0.74	0.59	0.95
P_2O_5	0.25	0.09	0.10	0.28	0.10	0.27	0.15	0.27	0.23	0.30	0.09
LOI	2.26	1.57	1.84	2.18	1.90	2.79	2.37	3.01	3.42	2.47	1.5
Mg#	49.70	26.50	28.7	50.40	28.7	50	29.4	50.90	43.90	50.70	26.10
AI	29.73	18.35	13.80	30.23	13.95	29.46	20.66	30.04	31.71	29.08	19.44
ASI	0.81	1.56	1.01	0.83	1.04	0.80	0.95	0.84	0.97	0.89	1.14
Li (ppm)	15.927	4.82	4.235	12.877	2.512	16.998	3.924	11.641	16.756	9.407	2.676
P	923.899	325.253	297.797	925.674	123.642	922.976	473.773	935.297	929.275	736.994	298.553
Sc	31.665	10.934	10.585	33.355	8.563	31.665	15.61	32.201	27.309	27.142	10.456
Ti	6186.03	2051.003	1945.523	6248.141	1130.25	6261.12	2823.324	6357.169	5675.727	5953.72	1933.763

Table 1. *Cont.*

Rock Type	Basalt	Dacite	Dacite	Basalt	Andesite	Basalt	Andesite	Basalt	Basalt	Basalt	Dacite
V	294.255	7.82	6.939	328.117	8.424	282.699	32.773	306.601	222.053	268.946	10.287
Cr	34.977	0.491	0.536	28.235	1.521	35.284	2.064	30.658	25.555	7.086	0.497
Co	40.842	20.738	29.545	35.459	27.978	42.531	27.896	36.953	46.008	35.93	33.04
Ni	16.879	1.167	1.095	12.824	1.753	17.929	2.124	14.605	14.883	6.945	1.072
Cu	78.022	4.701	0.783	77.554	4.979	77.621	15.722	75.727	71.05	58.641	7.747
Zn	91.768	99.132	64.873	88.96	120.768	92.939	97.457	94.3	88.436	102.137	79.323
Ga	17.126	16.607	15.765	19.103	14.935	16.722	16.765	17.444	16	16.928	16.092
AS	0.436	0.568	0.505	0.472	0.483	0.439	0.541	0.506	2.29	0.418	0.521
Rb	7.954	10.344	5.713	4.233	13.44	8.073	12.098	2.529	8.45	11.711	11.163
Sr	149.33	162.139	42.604	176.411	113.444	148.25	131.548	167.268	138.4	237.621	31.73
Y	15.697	44.227	50.845	14.877	40.086	16.043	34.221	16.376	15.533	24.315	42.815
Zr	19.001	222.455	223.21	27.82	139.132	16.111	110.988	26.95	28.934	44.585	216.571
Nb	3.514	10.36	9.416	4.574	4.774	4.118	7.964	3.451	3.655	4.769	9.435
Sn	1.467	2.966	2.882	1.049	1.558	1.559	1.943	0.958	0.63	1.346	2.519
Sb	0.536	0.409	0.204	1.786	0.111	0.386	0.571	1.128	2.238	0.627	0.15
Cs	0.049	0.119	0.085	0.073	0.029	0.058	1.203	0.047	0.051	0.084	0.044
Ba	227.327	413.464	301.865	165.894	267.374	216.201	383.92	156.334	275.752	281.047	528.082
La	8.245	20.264	19.316	8.589	11.515	8.018	16.053	8.133	11.109	9.843	22.643
Ce	17.154	44.169	42.305	17.887	26.379	17.256	35.999	18.479	23.503	22.248	50.004
Pr	2.678	5.68	5.477	2.762	3.662	2.328	4.607	2.489	2.691	2.97	6.111
Nd	11.125	25.375	25.575	12.247	17.81	11.071	20.989	11.806	12.616	14.21	26.624
Sm	3.102	6.466	6.223	3.097	4.922	2.854	5.402	3.028	3.062	3.81	6.442
Eu	1.224	1.42	1.317	1.156	1.221	1.115	1.628	1.238	1.144	1.379	1.395
Gd	2.956	7.318	7.393	3.122	6.038	3.171	6.163	3.313	3.275	4.378	7.229
Tb	0.587	1.214	1.266	0.478	1.033	0.486	1	0.507	0.489	0.706	1.183
Dy	3.203	8.214	8.734	3.178	7.059	3.056	6.593	3.249	3.045	4.69	7.925
Ho	0.757	1.751	1.885	0.643	1.498	0.625	1.374	0.653	0.616	0.963	1.69
Er	1.814	5.17	5.471	1.658	4.374	1.678	3.854	1.76	1.654	2.62	4.985
Tm	0.329	0.761	0.774	0.227	0.638	0.229	0.544	0.239	0.227	0.367	0.759
Yb	1.423	5.452	5.52	1.432	4.748	1.447	3.648	1.476	1.481	2.291	5.403
Lu	0.178	0.813	0.818	0.179	0.634	0.189	0.506	0.188	0.206	0.296	0.795
Hf	0.788	6.095	6.113	1.745	4.087	0.892	3.051	1.16	1.087	1.595	5.967
Ta	0.254	0.616	0.581	0.159	0.301	0.248	0.487	0.195	0.198	0.287	0.564
W	35.973	73.977	98.177	33.756	93.833	36.024	73.753	35.835	46.649	32.944	104.903
Pb	1.764	0.05	2.229	2.249	18.116	1.797	4.806	2.027	2.219	3.018	0.021
Th	0.345	3.114	2.886	0.344	1.29	0.326	2.013	0.313	0.303	0.998	4.754
U	0.162	2.985	1.206	0.247	0.611	0.152	0.786	0.154	0.141	0.407	2.772
La_N/Yb_N	4.16	2.67	2.51	4.30	1.74	3.97	3.16	3.95	5.38	3.08	3.01
Eu/Eu*	1.24	0.63	0.59	1.14	0.68	1.13	0.86	1.19	1.10	1.03	0.62
Nb/Nb*	0.71	0.45	0.43	0.87	0.42	0.86	0.47	0.73	0.68	0.52	0.40
Ti/Ti*	0.77	0.12	0.12	0.87	0.08	0.90	0.20	0.86	0.78	0.61	0.12
Hf/Hf*	0.28	2.72	2.42	0.58	1.81	0.32	1.05	0.40	0.41	0.46	2.63
Ce/Ce*	0.90	1.01	1.01	0.90	1.00	0.98	1.03	1.01	1.05	1.01	1.04

Mg# = molar ratio of [MgO/(MgO + FeO)] × 100); assuming FeOt = Fe_2O_3 × 0.8998Fe_2O_3; AI = [(MgO + K_2O)/(MgO + K_2O+ CaO + Na_2O)] × 100; ASI = [Al_2O_3/(CaO+ Na_2O + K_2O)] molar. (*) refer to normalizing values of Eu, Nb, Ti, Hf and Ce.

Table 2. Whole-rock major and trace element composition of Maroua volcanic rocks, Mount Mbalgaré.

Rock Type	Andesite	Dacite	Basalt	Dacite	Dacite	Basalt	Andesite	Basalt	Dacite	Andesite
Lon. (°E) Lat. (°N)	14.32875 10.61855	14.32836 10.62064	14.32909 10.62423	14.32863 10.62193	14.32879 10.62221	14.32959 10.62585	14.33079 10.62454	14.33070 10.62537	14.33132 10.62331	14.33183 10.62101
Sample ID	MB2	MB3	MB4	MB5	MB6	MB8	MB11	MB12	MB13	MB17
SiO_2 (Wt%)	73.13	75.25	60.17	73.39	74.92	49.88	72.43	60.40	73.72	74.64
TiO_2	0.30	0.19	1.05	0.24	0.20	1.28	0.28	0.97	0.23	0.26
Al_2O_3	13.55	12.34	15.45	13.12	12.57	18.69	13.82	14.91	13.22	13.04
Fe_2O_3	4.76	3.45	9.47	4.00	3.49	12.71	4.43	9.11	3.85	3.24
MnO	0.18	0.18	0.20	0.19	0.15	0.21	0.14	0.21	0.22	0.11
MgO	0.49	0.51	3.36	0.40	0.47	4.95	0.13	3.07	0.52	0.65
CaO	0.80	1.62	4.32	1.31	1.29	7.77	1.22	5.19	1.86	1.55
Na_2O	6.35	5.01	4.91	6.17	4.76	2.58	5.98	5.29	4.64	5.63
K_2O	0.36	1.41	0.75	1.15	2.09	1.72	1.51	0.52	1.68	0.81
P_2O_5	0.09	0.05	0.33	0.02	0.06	0.21	0.06	0.33	0.04	0.06
LOI	1.64	1.65	2.74	1.50	1.34	3.54	1.50	2.59	1.76	2.61
Mg#	18.70	24.90	44.40	18.3	23.2	46.70	6.2	43.10	23.20	31.10
AI	10.61	22.42	30.81	17.15	29.67	39.18	18.49	25.50	25.29	16.87
ASI	1.10	0.97	0.92	0.95	1.01	0.92	1.01	0.80	1.03	1.01
Li (ppm)	5.628	4.586	6.277	2.642	2.724	10.4	1.758	4.109	3.225	5.132
P	267.841	304.396	1073.705	144.781	143.745	646.183	147.295	995.549	120.828	178.029
Sc	16.013	11.132	27.407	11.705	9.686	31.062	13.359	27.229	12.107	10.578
Ti	1686.701	1968.293	5966.2	1367.586	1197.843	7490.188	1591.574	5552.291	1341.177	1375.951
V	0.87	6.971	152.985	6.971	10.574	379.948	0.145	158.208	7.287	14.35
Cr	0.658	0.622	0.467	1.5	1.685	4.611	0.508	2.113	1.504	1.842
Co	17.253	35.159	26.209	25.474	28.941	44.23	26.63	32.819	22.356	35.095
Ni	0.726	1.133	0.831	1.461	1.597	10.943	0.801	1.389	1.513	1.62
Cu	1.558	1.169	4.29	3.24	4.251	175.571	0.642	5.833	4.78	7.818
Zn	102.391	69.102	90.542	120.788	88.372	94.918	107.682	95.773	110.56	68.281
Ga	15.056	15.807	14.373	16.451	14.782	16.219	16.722	15.507	16.432	11.666
AS	0.417	0.457	0.45	0.5	0.473	0.17	0.525	0.231	0.442	0.831
Rb	3.614	5.374	6.127	11.716	20.978	19.097	11.314	5.083	15.37	9.242
Sr	55.379	44.665	176.421	70.998	160.814	357.882	123.885	95.015	116.067	72.274
Y	29.461	39.152	21.726	42.945	38.952	12.765	42.423	19.457	41.063	28.967
Zr	98.986	223.897	44.427	126.069	95.479	30.368	94.92	25.07	102.322	114.415
Nb	2.593	9.417	1.7	5.237	4.819	1.391	5.99	1.544	4.976	2.753
Sn	1.314	2.05	1.433	1.983	1.936	0.458	1.532	0.646	1.848	1.247
Sb	0.267	0.174	0.266	0.074	0.14	0.101	0.129	0.111	0.118	0.1
Cs	0.037	0.086	0.042	0.117	0.053	0.087	0.029	0.388	0.028	0.155
Ba	160.748	284.24	479.863	206.581	532.929	1030.16	478.942	264.699	343.072	385.587
La	7.226	16.503	5.591	14.903	12.66	4.516	16.346	4.925	14.075	7.637
Ce	18.841	37.582	13.778	33.369	30.324	9.885	34.048	12.171	31.545	16.096
Pr	2.691	4.98	2.069	4.539	4.206	1.46	5.172	1.782	4.469	2.241
Nd	13.442	21.946	10.797	21.841	20.082	7.436	24.74	9.292	21.565	10.243
Sm	3.859	5.49	3.179	6.018	5.489	2.098	6.553	2.712	5.854	2.777
Eu	1.209	1.167	1.226	1.74	1.422	1.007	1.816	1.072	1.664	0.86
Gd	4.708	6.087	3.915	7.184	6.445	2.494	7.66	3.396	7.025	3.773
Tb	0.798	0.999	0.625	1.214	1.098	0.394	1.26	0.554	1.197	0.67
Dy	5.483	6.82	4.219	8.263	7.464	2.535	8.397	3.62	8.019	4.759
Ho	1.183	1.486	0.874	1.74	1.573	0.518	1.738	0.761	1.666	1.054
Er	3.48	4.754	2.463	4.915	4.362	1.408	4.85	2.144	4.682	3.25
Tm	0.524	0.749	0.348	0.707	0.615	0.194	0.683	0.304	0.669	0.486
Yb	3.679	5.553	2.376	4.784	4.057	1.275	4.542	2.16	4.679	3.619

Table 2. *Cont.*

Rock Type	Andesite	Dacite	Basalt	Dacite	Dacite	Basalt	Andesite	Basalt	Dacite	Andesite
Lu	0.543	0.818	0.32	0.663	0.515	0.176	0.556	0.282	0.579	0.504
Hf	2.9	6.439	1.363	3.87	3.025	0.933	2.928	0.933	3.145	3.441
Ta	0.176	0.595	0.119	0.324	0.295	0.094	0.355	0.106	0.297	0.184
W	55.816	120.601	34.449	86.077	92.281	29.777	107.456	66.165	82.66	123.004
Pb	0	0.04	0.756	3.736	4.472	1.139	1.434	1.131	0.21	0.084
Th	3.009	2.119	0.414	1.352	1.249	0.255	1.271	0.37	3.538	1.58
U	0.8	2.886	0.297	0.618	0.561	0.126	0.5	0.22	1.234	0.963
La_N/Yb_N	1.41	2.13	1.69	2.23	2.24	2.54	2.58	1.64	2.16	1.51
Eu/Eu*	0.62	0.87	1.06	0.81	0.73	1.35	0.78	1.08	0.79	0.81
Nb/Nb*	0.37	0.46	0.38	0.40	0.41	0.44	0.45	0.39	0.40	0.34
Ti/Ti*	0.16	0.14	0.71	0.09	0.08	1.39	0.09	0.76	0.09	0.17
Hf/Hf*	1.08	1.96	0.41	3.14	1.67	0.44	1.41	0.30	0.84	1.88
Ce/Ce*	1.05	1.02	0.99	0.99	1.02	0.94	0.91	1.01	0.98	0.95

Mg# = molar ratio of [MgO/(MgO + FeO)] × 100); assuming FeOt = Fe_2O_3 × 0.8998Fe_2O_3; AI = [(MgO + K_2O)/(MgO + K_2O+ CaO + Na_2O)] × 100; ASI = [Al_2O_3/(CaO+ Na_2O + K_2O)] molar. (*) refer to normalizing values of Eu, Nb, Ti, Hf and Ce.

4.1.1. Major Elements

To minimize the effects of alteration on the samples, the concentrations of major element oxides in the studied lavas were recalculated to 100% on an anhydrous basis. Mg# was calculated as the mole ratio of MgO/(MgO + FeO), assuming FeOt = Fe_2O_3 × 0.8998 Fe_2O_3. The mafic rocks showed a wide range in their MgO (3.07–5.04 wt%), TiO_2 (0.96–1.28 wt%) and Fe_2O_3 (9.11–12.71 wt%) contents, with a Mg number (Mg#) varying from 43.10 to 50.90.

The felsic lavas, on the other hand, were characterized by low MgO (0.13–1.08 wt%), TiO_2 (0.19–0.50 wt%) and Fe_2O_3 (3.24–5.81 wt%) contents and a low Mg# (6–31.10). In the Harker diagrams of major element oxide content against SiO_2 concentration (Figure 6a–f), the concentrations of Fe_2O_3, TiO_2, Al_2O_3, MgO, P_2O_5 and CaO decrease from basalts to dacites. The Na_2O and K_2O values, on the other hand, rise in the mafic samples and then decrease abruptly in the felsic samples (Figure 6g,h).

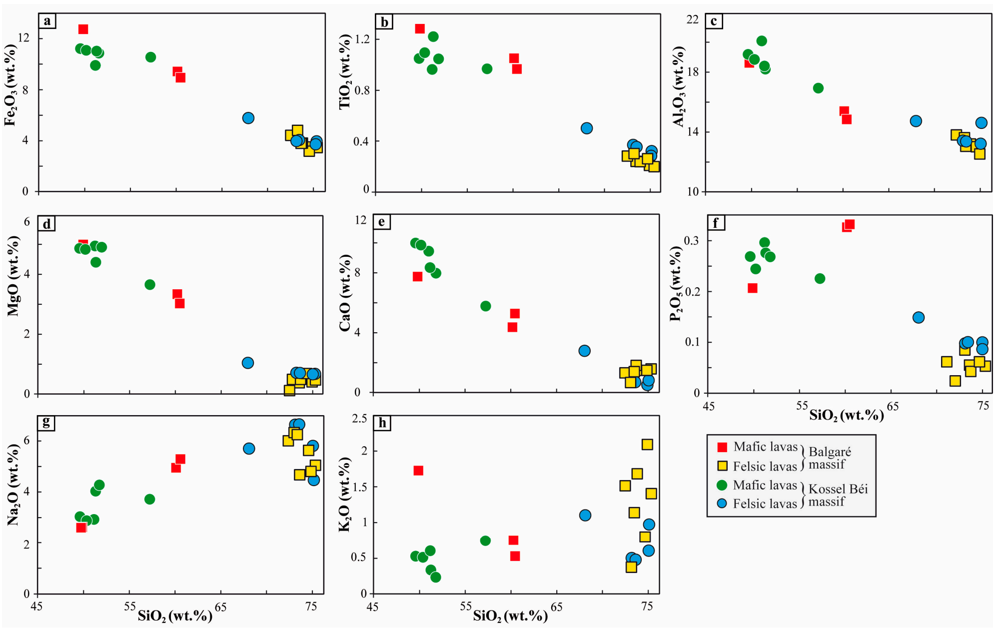

Figure 6. Harker diagrams showing the content of major element oxides ((**a**) Fe_2O_3; (**b**) TiO_2; (**c**) Al_2O_3; (**d**) MgO; (**e**) CaO; (**f**) P_2O_5; (**g**) Na_2O; (**h**) K_2O) vs. SiO_2 concentration.

4.1.2. Trace Elements

The contents of the compatible trace elements Sc, Ni, Co and Cr ranged from 27.14 to 33.36 ppm, 0.73 to 17.93 ppm, 26.21 to 46.01 ppm and 0.47 to 35.28 ppm, respectively, in the mafic lavas, while for the felsic samples, these concentrations were relatively low (8.56–16.01 ppm, 0.73–2.12 ppm, 17.25–35.16 ppm and 0.49–2.06 ppm).

The concentrations of the incompatible trace elements Zr, Nb and La varied widely between the mafic lavas (16.11–44.59 ppm, 1.36–4.77 ppm and 4.52–11.11 ppm, respectively) and the felsic rocks (94.92–223.90 ppm, 2.59–10.36 ppm and 7.23–22.64 ppm, respectively). The plots of selected trace element content vs. SiO_2 concentration display negative correlations, with a continuous decrease in Sc, Ni, V and Sr concentrations (Figure 7a–d). Positive correlations were observed with increasing Zr, Nb, Ba and La contents (Figure 7e–h). In Figure 8, the concentrations of the selected rare earth elements (REEs) and trace elements are normalized to those of chondrite and primitive mantle according to [39] and specified, respectively, by the (N) and (PM) subscripts. On the chondrite-normalized REE diagram, mafic and felsic rocks display fractionated patterns with enrichment in the light REEs and depletion of the heavy REEs (Figure 8a,b; La_N/Yb_N = 1.41–5.38). The felsic samples display a negative Eu anomaly ($Eu/Eu^* = Eu_N/(Sm_N \times Gd_N)^{1/2}$ = 0.59–0.87), while the mafic lavas exhibit practically no or a positive Eu anomaly (Eu/Eu^* = 1.03–1.35). There are no obvious Ce anomalies (Ce/Ce^* = 0.9–1.05) in any of the samples. On the primitive mantle-normalized trace element diagram, the rocks show negative Ti and Nb–Ta anomalies for most samples (0.08–0.9 and 0.54–0.74, respectively) and negative (0.28–0.58 for mafic samples) to positive (1.05–3.14 for felsic samples) Hf–Zr anomalies.

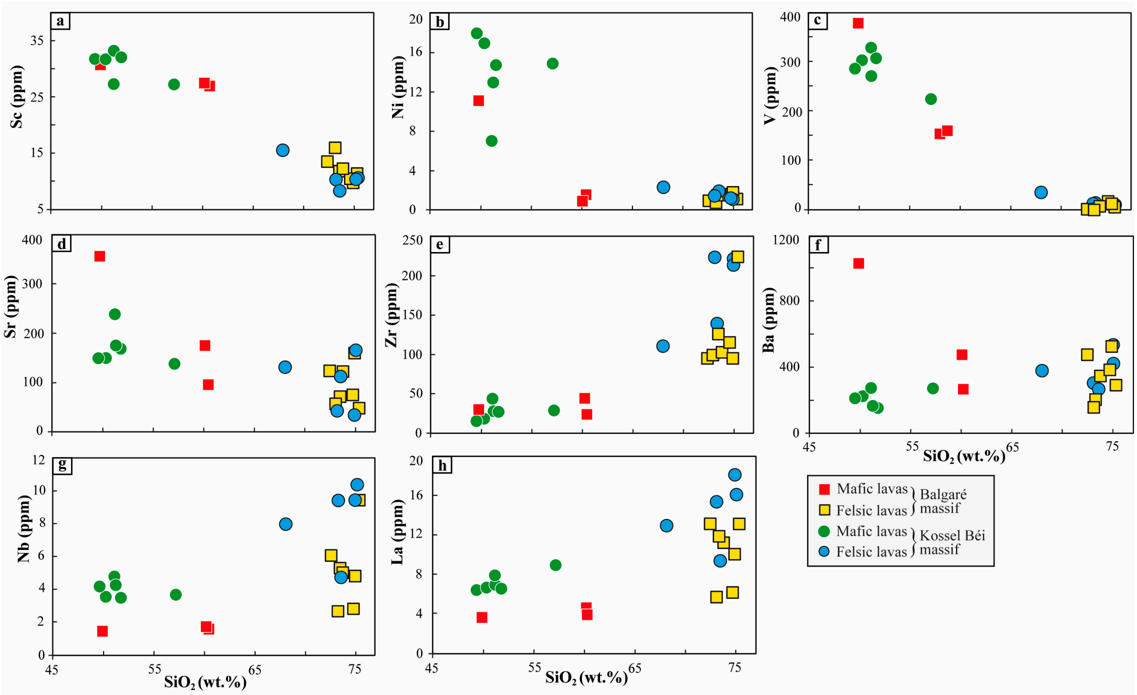

Figure 7. Harker diagrams showing selected trace elements ((**a**) Sc; (**b**) Ni; (**c**) V; (**d**) Sr; (**e**) Zr; (**f**) Ba; (**g**) Nb; (**h**) La) vs. SiO_2 concentration.

5. Discussion

5.1. Assessment of Alteration and Trace Element Mobility

The relatively high loss on ignition (LOI) values of the volcanic rocks of Maroua (1.34–3.54 wt%) are consistent with the fact that the samples were altered. In addition to geochemical alteration, the studied rocks underwent post-magmatic metamorphic processes, and therefore, an assessment of the degree of trace element mobility was important before any petrogenetic interpretation of such rocks. The Alumina Saturation Index (ASI) and the Alteration Index (AI) are good indicators to evaluate the intensity of weathering that has affected magmatic rocks. Unaltered island-arc basalts and mid-ocean-ridge basalts have average AI values of 34 ± 10% and 36 ± 8%, respectively [40]. In contrast, ASI values >1 are due to alkali loss and linked to hydration and/or alteration [41]. All samples of Mts. Kossel Béi and Mbalgaré exhibited ASI values between 0.80 and 1.1 (Table 1) and AI values between 10.61% and 39.18% (Table 1), suggesting that they were somewhat fresh and thus had not undergone significant alteration.

Earlier studies (e.g., [42–44]) revealed that mobile elements, such as K, Fe, Na, Ca, P, Rb, Ba, Sr and Cs, are alteration-sensitive and could be mobilized during metamorphism and post-magmatic crystallization. Some elements are known to remain generally immobile during alteration and metamorphism up to amphibolite facies, i.e., Ti, Al, Cr, Ni, V, Sc, Nb, Zr, Ta, Hf, Y, Th, Sm and the heavy REEs (e.g., [45]) and were thus considered suitable for the petrogenetic interpretation of the Maroua volcanic rocks. Furthermore, the robust correlations in the Harker diagrams (Figures 6 and 7) and the coherent presentation of the REE and trace element patterns (Figure 8) without any noticeable Ce anomalies (e.g., [46]) were taken as evidence that the major elements, trace elements and light REEs were not significantly mobilized during the low-grade metamorphism and post-magmatic alteration.

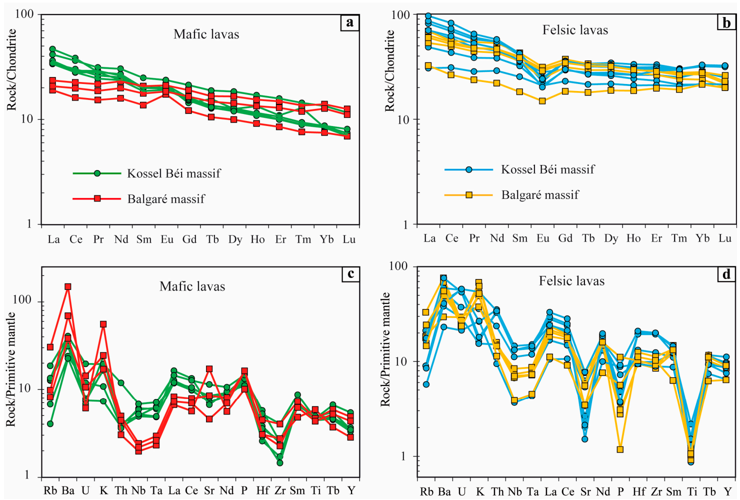

Figure 8. (**a**,**b**) Chondrite-normalized rare earth element (REE) diagrams and (**c**,**d**) primitive mantle-normalized multi-element diagrams for the Maroua volcanic rocks. Normalizing values are from [41].

5.2. Fractional Crystallization

The relatively low and wide range of Mg# (6.2–50.9) and MgO (0.13–4.95 wt%), Ni (0.73−17.93 ppm), Co (17.25−46.01) and Cr (0.47−35.28) contents shown by the Maroua volcanic rocks suggest that they do not represent compositions of a primitive magma. Instead, these characteristics imply that they underwent extensive fractional crystallization (FC) from primary magmas either en route to the surface or in magma chambers [47]. This primitive magma generally has Mg# of 68–72 and very high abundances of these components: MgO > 10 wt%; Ni, 300–400 ppm; Co, 50–70 ppm; and Cr, 300–500 ppm [48,49]. FC played an important role in the differentiation of the Maroua lavas, as evidenced by the robust correlation in the Harker diagrams and trace element distribution patterns. The Yb vs. La/Yb and Zr/Nb vs. Ba/La diagrams (Figure 9a,b) also confirmed that crystal fractionation played a significant role in the genesis of these rocks. The decrease in Fe_2O_3 and TiO_2 with SiO_2 (Figure 6a,b) indicates a stage of fractionation of Fe-Ti oxide minerals during magmatic differentiation. The FC of olivine in mafic samples is inferred from the decreasing Ni (Figure 7b) and MgO (Figure 6d) concentrations with increasing silica content, whereas the crystal fractionation of clinopyroxene is evidenced by a decrease in the CaO and Sc (Figures 6e and 7a) contents with increasing SiO_2 content. The negative correlation between Dy/Yb ratios and SiO_2 content (Figure 9c) illustrates the fractionation of amphibole rather than clinopyroxene in most of the volcanic rocks. The increase in K_2O and Na_2O concentrations with differentiation, along with the significant variation of the Ba/La ratios (13.86–50.49) and the constant values of Y/Nb (4.27–8.4) in the felsic lavas, could be attributed to an important alkali feldspar fractionation at the end of the FC process [50,51]. The decrease in CaO and Sr content with that of SiO_2, combined with Sr and Eu anomalies, particularly in the most differentiated rocks, is consistent with the fractionation of plagioclase. The plot of Sr vs. Rb/Sr (Figure 9d) with a negative correlation also illustrates that the fractionation of K-feldspar and plagioclase was the principal mechanism in the course of magmatic differentiation. The volcanic rocks outcropping in Mts. Kossel Béi and Mbalgaré presented clear linear correlations on the Harker diagrams (Figures 6 and 7), suggesting that the felsic rocks were derived from more basaltic parental magmas by fractional crystallization.

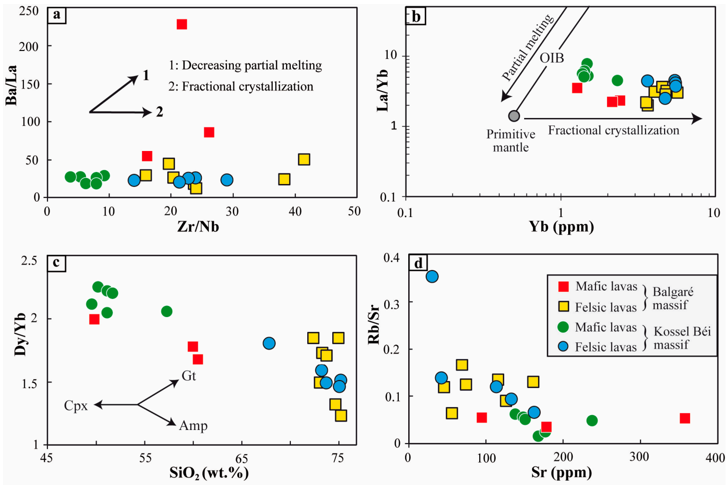

Figure 9. (**a**) Zr/Nb vs. Ba/La (after [52]) and (**b**) Yb vs. La/Yb (after [53]) plots of fractional crystallization as the main petrogenetic process for the studied rocks. (**c**) Plot of SiO_2 concentration vs. Dy/Yb showing abundant crystallization of amphibole rather than clinopyroxene (after [54]). (**d**) Binary Sr vs. Rb/Sr plot showing a negative correlation and illustrating K-feldspar and plagioclase fractionation. Cpx: clinopyroxene; Gt: garnet; Amp: amphibole; OIB: oceanic island basalt.

5.3. Source Characteristics, Tectonic Setting and Geodynamic Model

Before characterizing the magmatic source of the studied rocks, it was important to check whether this magma had not been contaminated during its ascent by crustal material. The Nb/Yb vs. Th/Yb crustal input plot (Figure 10a) [55] shows that the majority of the samples are displaced off the MORB-OIB-OPB primitive array, indicating some enrichment in crustal material. The MORB-OIB-OPB primitive array contains nearly all of the mafic lavas from the Kossel Béi Mountain, which suggests that they are uncontaminated lavas. The Nb/Yb vs. TiO_2/Yb diagram (Figure 10b) [55] also shows the group of uncontaminated mafic lavas, which correspond to the tholeiitic series, as previously indicated in Figure 3b. The great majority of the Kossel Béi mafic lavas on the Nb/U vs. Ce/Pb diagram [56] (Figure 10c) are plotted far from Precambrian basement samples [57], thus reflecting the fact that the source magma of these rocks was less contaminated by crustal components. Furthermore, compared to felsic lavas (positive Zr-Hf anomaly: 1.08–3.14; high Zr/Sm: 14.48–41.2), these mafic samples were characterized by negative Zr-Hf anomalies (0.28–0.58) and low Zr/Sm ratios (5.65–9.45), which therefore suggests very limited crustal contamination [58–60]. In the Nb/La vs. La/Yb plots [61] of the Maroua volcanic rocks (Figure 10d), the values of Nb/La vary from 0.30 to 0.57, which brings them closer to the field of the average lower crust, thus indicating a lithospheric mantle source for most of the studied rocks. It is worth noting that the uncontaminated mafic samples plotted near the limit of the lithospheric mantle and the zone of lithosphere–asthenosphere interaction, thus reflecting the fact that the mafic magma was more or less contaminated by crustal material, albeit to a limited extent.

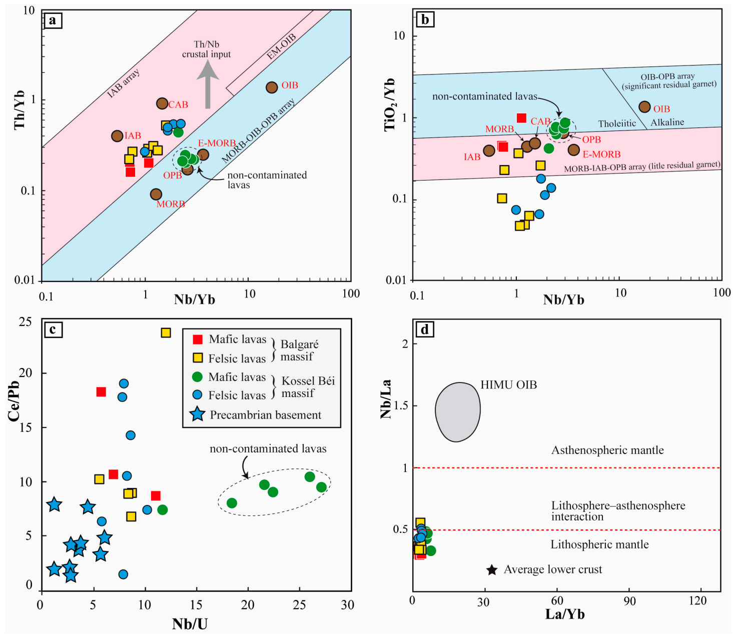

Figure 10. (**a**) Nb/Yb vs. Th/Yb diagram [55] illustrating crustal input projection, where higher Th/Nb ratios indicate more crustal contamination; the non-contaminated mafic lavas of Mt. Kossel Béi plot between E-MORB and OPB; (**b**) TiO_2/Yb-Nb/Yb diagram [55] showing residual garnet projection in the source; (**c**) Ce/Pb vs. Nb/U plots after [56]. The data for the Precambrian basement are from [57]. (**d**) Nb/La vs. La/Yb plots of the Maroua volcanics [61]. OIB: oceanic island basalt; MORB: mid-ocean-ridge basalt; E-MORB: enriched mid-ocean-ridge basalt; IAB: island-arc basalt; EM-OIB: enriched-mantle ocean island basalt; CAB: continental-arc basalt; OPB: oceanic-plateau basalt.

Using these five (5) mafic samples, which were significantly less contaminated than the others, the mineralogical composition and the melting degree of the source of the Maroua volcanic rocks could be modelled on REE ratio plots from the melting equations [62]. The presence of garnet in the mantle source of the studied rocks was characterized by Dy/Yb > 2 (2.00–2.94) for these mafic uncontaminated samples [63,64] (Figure 11a).

According to [65], the presence of a garnet phase in the source was also suggested by the enrichment in LREE over HREE, since garnet has an important HREE affinity and depletes these elements from melts. The Sm/Yb vs. La/Sm variation diagram [66] (Figure 11b) confirmed the presence of residual garnet in the mantle source of the studied Maroua rocks. The REE patterns of the mafic samples presented a negative slope (Figure 8a) and probably indicated their origin from a relatively low degree of partial melting from an enriched mantle source. In Figure 11b, this percentage of partial melting fluctuates between 5 and 10%.

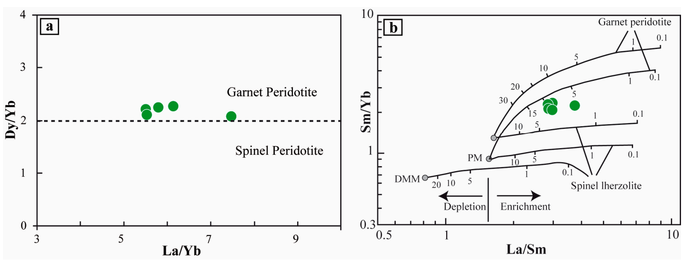

Figure 11. Plots of uncontaminated mafic lavas of Mt. Kossel Béi in the (**a**) Dy/Yb vs. La/Yb diagram (after [63,64]) and (**b**) Sm/Yb vs. La/Sm diagram (after [66]). PM: primitive mantle; DMM: depleted MORB mantle.

The Maroua volcanic rocks showed a negative slope from LILE (Ba, K and Th) to HFSE (Nb, Hf, and Ti) on the primitive mantle-normalized spider diagrams and presented negative Eu anomalies for the felsic lavas. These geochemical features are compatible with those of subduction-related magmas [67] and active continental margins [68,69]. The negative anomalies of Nb-Ta and Zr-Hf on the multi-element spider diagrams also suggest contributions or interactions of a pre-existing subducted crustal component or assimilation of the upper crust by the magma. Figure 12 displays geotectonic discriminant diagrams of the Maroua volcanics. On the La/10-Y/15-Nb/8 diagram [70], the rocks plot in the syn- to post-orogenic, active margin setting (Figure 12a). In the Th-Ta-Hf/3 triangular diagram (Figure 12b) [71], the samples fall in the volcanic arc field or the supra-subduction-zone basalt field. The Y vs. Zr plot (Figure 12c) [72] also illustrates the fact that the Maroua metavolcanic rocks belong to the fields of arc-related active margin settings. In the Y vs. Nb and Y + Nb vs. Rb diagrams [69], all the investigated samples fall within the volcanic arc granite field (Figure 12d,e). The Th/Nb vs. Ba/Th diagram (Figure 12f) [73] shows that the studied samples plotted toward the subducted slab-derived fluid. Therefore, the parental magma of the Maroua volcanic samples was probably generated during the interaction between the subducted crustal components and the lithospheric mantle, as previously suggested.

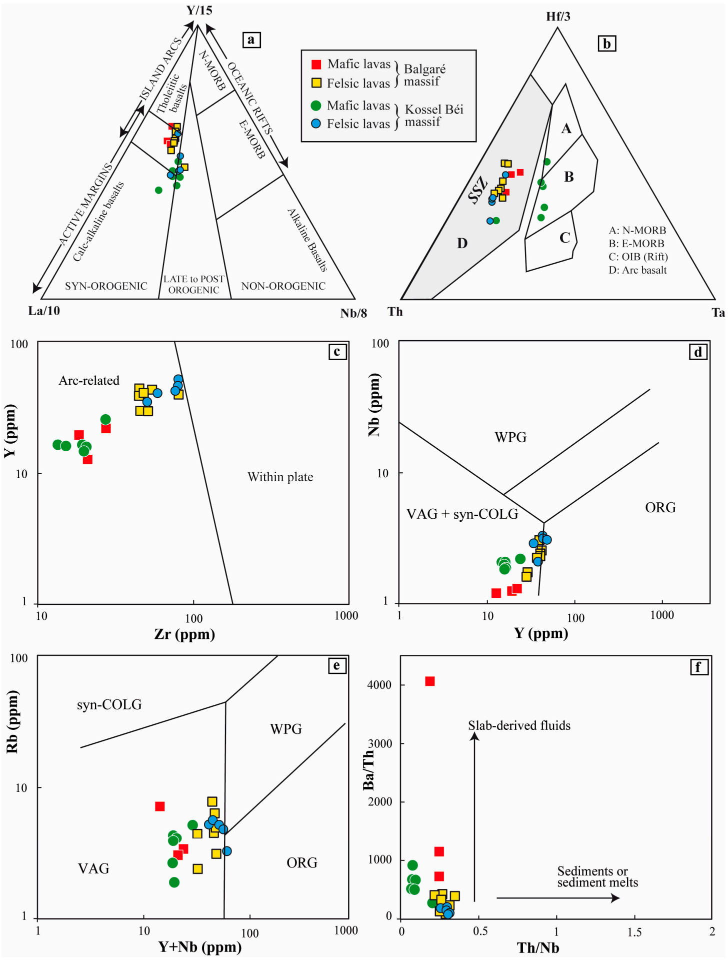

Figure 12. Geotectonic discriminant diagrams of the Maroua volcanics. (**a**) La/10-Nb/8-Y/15 diagram [70]; (**b**) Th-Hf/3-Ta diagram [71]; (**c**) Y vs. Zr diagram after [72]; (**d**) Y vs. Nb and (**e**) Y + Nb vs. Rb diagrams after [69]; (**f**) Th/Nb vs. Ba/Th diagram after [73]. Primitive-mantle normalizing values were from [74]. SSZ: supra-subduction-zone basalts; VAG: volcanic-arc granitoids; syn-COLG: syn-collisional granitoids; WPG: within-plate granitoids; ORG: oceanic-ridge granitoids.

Figure 13 proposes a geodynamic model comprising different stages that led to the emplacement of the Maroua volcanic rocks. The increase in the dip angle of the subducted slab following the convergence of the Congo craton (Adamawa-Yadé Domain) and the Saharan craton (Western Cameroon Domain) resulted in lithospheric thinning via extension, which caused slab detachment, upwelling and slab melting of the asthenosphere. The partial melting of the enriched lithospheric mantle, with input of lower continental crust, then generated the primary mafic magmas, which produced the volcanic rocks of Maroua through fractional crystallization.

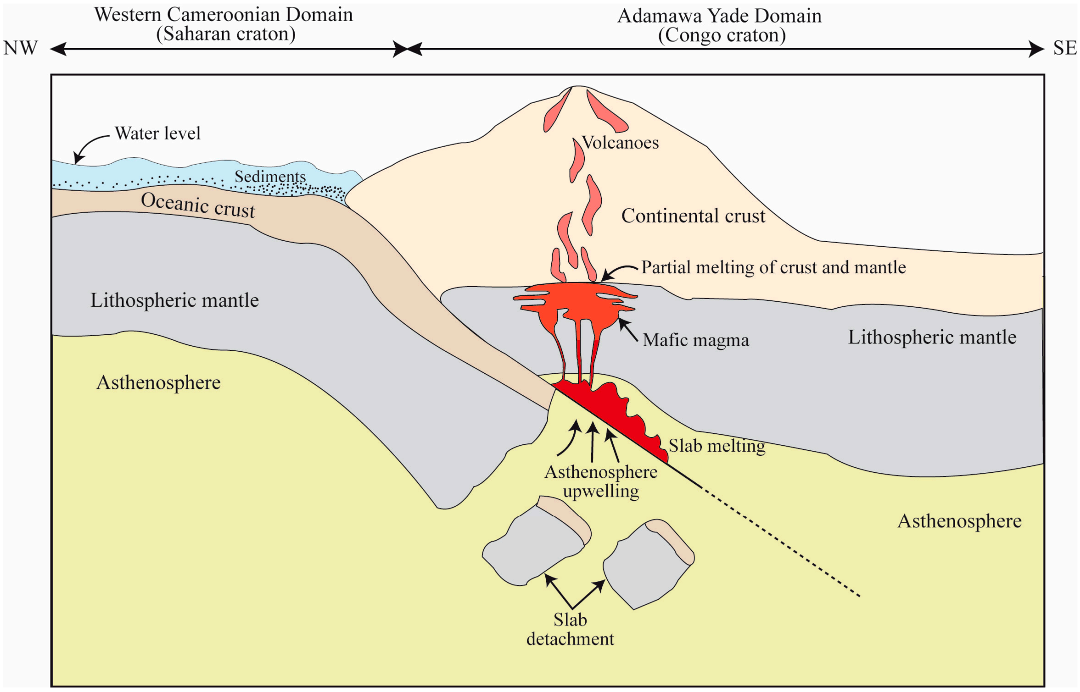

Figure 13. Schematic geotectonic model for the genesis of the Maroua volcanic rocks (adapted from [7]). The color of melts generated from the slab melting, partial melting of crust and mantle, and welling magma in the continental crust are different because their composition are evolutionary.

6. Conclusions

The Maroua metavolcanic rocks are located at the northern margin of the Central African Fold Belt in northern Cameroon and include basalts, andesites and dacites. The chemistry of the studied rocks showed that the mafic samples are essentially magnesian, whereas the felsic rocks are ferroan and belong to the calc-alkaline medium-K and, mainly, low-K tholeiite series. Major and trace element systematics of the volcanic rocks suggest that the lavas originate from a similar mantle source with compositional variations mainly caused by fractional crystallization. The modelled results indicate a derivation of the studied rocks from primitive parental melts generated by the 5–10% partial melting of a source containing garnet peridotite, probably generated during the interaction between the subducted oceanic crust and the lithospheric mantle and which evolved chemically through fractional crystallization and assimilation. The features exhibited by the studied rocks are similar to those of subduction-zone melts and are characterized by the fact that on chondrite-normalized REE diagrams and primitive mantle-normalized spidergrams, (i) the mafic and felsic rocks display fractionated patterns with enrichment in the light REEs and depletion of the heavy REEs (LaN/YbN = 1.41–5.38); (ii) negative Nb–Ta (0.54–0.74), Ti (0.08–0.9) and Eu (0.59–0.87) anomalies were found for most samples.

Author Contributions: Conceptualization, P.C.B.à.N. and M.G.D.; methodology, P.C.B.à.N., M.G.D., D.H.D., N.L., M.N.K., P.M.F.T. and P.K.; validation, P.C.B.à.N., M.G.D. and N.L.; formal analysis, P.C.B.à.N., M.G.D., D.H.D., N.L., M.N.K. and P.M.F.T.; investigation, P.C.B.à.N., M.G.D. and N.L.; resources, P.C.B.à.N., M.G.D. and N.L.; data curation, P.C.B.a.N., M.G.D., P.K. and N.L.; writing—original draft preparation, P.C.B.à.N., M.G.D. and N.L.; writing—review and editing, P.C.B.à.N., M.G.D., D.H.D., N.L., M.N.K., P.M.F.T. and P.K.; supervision, M.G.D., N.L. and P.K.; project administration, M.G.D. All authors have read and agreed to the published version of the manuscript.

Funding: This research received no external funding.

Data Availability Statement: The original contributions presented in the study are included in the article and further inquiries can be directed to the corresponding author.

Acknowledgments: The authors would like to warmly thank the anonymous reviewers for their comments, which deeply improved the paper.

Conflicts of Interest: The authors declare no conflicts of interest.

References

1. Toteu, S.F.; de Wit, M.; Penaye, J.; Drost, K.; Tait, J.A.; Bouyo Houketchang, M.; Van Schmus, W.R.; Jelsma, H.; Moloto-A-Kenguemba, G.R.; da Silva Filho, A.F.; et al. Geochronology and correlations in the Central African Fold Belt along the northern edge of the Congo Craton: New insights from U-Pb dating of zircons from Cameroon, Central African Republic, and south-western Chad. *Gondwana Res.* **2022**, *107*, 296–324. [CrossRef]
2. Villeneuve, M.; Gärtner, A.; Kalikone, C.; Wazi, N. Evolution Géodynamique de la chaine « Kibarienne » d'Afrique Centrale au Mésoprotérozoïque. *Pangaea Infos* **2019**, *15*, 4.
3. Collins, A.S.; Clark, C.; Sajeev, K.; Santosh, M.; Kelsey, D.E.; Hand, M. Passage through India: The Mozambique Palghat–Cauvery Ocean suture, high pressure granulites and the shear system. *Terra Nova.* **2007**, *19*, 141–147. [CrossRef]
4. Ngako, V.; Njonfang, E. Plates amalgamation and plate destruction, the Western Gondwana history. In *Tectonics*; INTECH: London, UK, 2011; 34p.
5. Isseini, M.; André-Mayer, A.S.; Vanderhaeghe, O.; Barbey, P.; Deloule, E. A-type granites from the Pan-African Orogenic Belt in magmas from different asthenospheric and lithospheric mantle sources. *J. Petrol.* **2012**, *1*, 351–377.
6. Bouyo Houketchang, M.; Penaye, J.; Barbey, P.; Toteu, S.F.; Wandji, P. Petrology of high-pressure granulite facies metapelites and metabasites from Tchollíré and Banyo regions: Geodynamic implication for the Central African Fold Belt (CAFB) of north-central Cameroon. *Precambrian Res.* **2013**, *224*, 412–433. [CrossRef]
7. Bouyo Houketchang, M.; Zhao, Y.; Penaye, J.; Zhang, S.H.; Njel, U.O. Neoproterozoic subduction-related metavolcanic and metasedimentary rocks from the Rey Bouba Greenstone Belt of north-central Cameroon in the Central African Fold Belt: New insights into a continental arc geodynamic setting. *Precambrian Res.* **2015**, *261*, 40–53. [CrossRef]
8. Toteu, S.F.; Yongue Fouateu, R.; Penaye, J.; Tchakounté, J.; Semo Mouangue, C.A.; Van Schmus, R.W.; Deloule, E.; Stendal, H. U-Pb dating of plutonic rocks involved in the nappe tectonic in Southern Cameroon: Consequence for the Pan-African orogenic evolution of the central African fold belt. *J. Afr. Earth Sci.* **2006**, *44*, 479–493. [CrossRef]
9. Njel, U.O. Paléogéographie d'un segment de l'orogenèse panafricaine: La ceinture volcano-sédimentaire de Poli (Nord Cameroun). *Comptes Rendus de l'Académie des Sciences. Série 2, Mécanique, Physique, Chimie, Sciences de l'univers, Sciences de la Terre* **1986**, *303*, 1737–1742.
10. Toteu, S.F. Geochemical characterization of the main petrographical and structural units of northern Cameroon: Implications for Pan-African evolution. *J. Afr. Earth Sci.* **1990**, *10*, 615–624. [CrossRef]
11. Toteu, S.F.; Michard, A.; Bertrand, J.M.; Rocci, G. U–Pb dating of Precambrian rocks from northern Cameroon, orogenic evolution and chronology of the Pan- African belt of central Africa. *Precambrian Res.* **1987**, *37*, 71–87. [CrossRef]
12. Doumnang, J.-C. Géologie des Formations Néoprotérozoïques du Mayo Kebbi (Sud-Ouest du Tchad): Apports de la Pétrologie et de la Géochimie, Implications sur la Géodynamique au Panafricain. Ph.D. Thesis, Université d'Orléans, Orléans, France, 2006.
13. Isseini, M. Croissance et Différenciation Crustales au Néoprotérozoïque: Exemple du Domaine Panafricain du Mayo Kebbi au Sud-Ouest du Tchad. Ph.D. Thesis, Université Henri Poincaré, Nancy I, Nancy, France, 2011.
14. Pinna, P.; Calvez, J.-Y.; Abessolo, A.; Angel, J.-M.; Mekoulou-Mekoulou, T.; Mananga, G.; Vernhet, Y. Neoproterozoic events in the Tchollíré area: Pan-African crustal growth and geodynamics in central-northern Cameroon (Adamawa and North Provinces). *J. Afr. Earth Sci.* **1994**, *18*, 347–353. [CrossRef]
15. Pouclet, A.; Vidal, M.; Doumnang, J.C.; Vicat, J.P.; Tchameni, R. Neoproterozoic crustal evolution in Southern Chad: Pan-African ocean basin closing, arc accretion and late- to post-orogenic granitic intrusion. *J. Afr. Earth Sci.* **2006**, *44*, 543–560. [CrossRef]
16. Penaye, J.; Kröner, A.; Toteu, S.F.; Van Schumus, W.R.; Doumnang, J.C. Evolution of the Mayo Kebbi region as revealed by zircon dating: An early (ca. 740 Ma) Pan-African magmatic arc in south-western Chad. *J. Afr. Earth Sci.* **2006**, *44*, 530–542. [CrossRef]
17. Lasserre, M.; Soba, D. Migmatisation d'âge panafricain au sein des formations Camerounaises appartenant à la zone mobile de l'Afrique centrale. *Comptes Rendus Sommaire de la Société Géologique de France* **1979**, *2*, 64–68.
18. Bessole, B.; Trompette, R. *Géologie d'Afrique. La Chaîne Panafricaine. "Zone Mobile d'Afrique Centrale (Partie Sud) et Zone Soudanaise*; Bureau de Recherches Géologiques et Minières: Orléans, France, 1980.
19. Ngako, V. Les Déformations Continentales Panafricaines en Afrique Centrale. Résultat d'un Poinçonnement de Type Himalayen. Ph.D. Thesis, Université de Yaoundé I, Yaoundé, Cameroun, 1999.
20. Ngnotué, T.; Nzenti, J.P.; Barbey, P.; Tchoua, F.M. The Ntui-betamba High-grade gneiss: A northward extension of the Pan-African Yaoundé gneiss in Cameroon. *J. Afr. Earth Sci.* **2000**, *2*, 369–381. [CrossRef]
21. Toteu, S.F.; Van Schmus, R.W.; Penaye, J.; Michard, A. New U–Pb and Sm–Nd data from North-Central Cameroon and its bearing on the Pre-Pan-African history of Central Africa. *Precambrian Res.* **2001**, *108*, 45–73. [CrossRef]

22. Ngako, V.; Affaton, P.; Njonfang, E. Pan-African tectonic in northwestern Cameroon: Implication for historyof westen Gondwana. *Gondwana Res.* **2008**, *14*, 509–522. [CrossRef]
23. Ngako, V.; Affaton, P.; Nnange, J.M.; Njanko, T. Pan-African tectonic evolution in central and southern Cameroon: Transpression and transtension during sinistral shear movements. *J. Afr. Earth Sci.* **2003**, *36*, 207–214. [CrossRef]
24. Caby, R.; Sial, A.N.; Arthaud, M.; Vauchez, A. Crustal evolution and the Braziliano orogeny in northeast Brazil. In *Orogens, The West African, Correlatives, Circum-Atlantic*; Dallmeyer, R.D., Lecorche, J.C.P.L., Eds.; Springer: Berlin/Heidelberg, Germany, 1991; pp. 373–397.
25. Abdelsalam, M.G.; Gao, S.S.; Liégeois, J.-P. Upper mantle structure of the Saharan Metacraton. *J. Afr. Earth Sci.* **2011**, *60*, 328–336. [CrossRef]
26. Nzenti, J.P.; Barbey, P.; Macaudiere, J.P.; Soba, D. Origin and evolution of the late Precambrian high grade Yaoundé gneisses (Cameroon). *Precambr. Res.* **1988**, *38*, 91–109. [CrossRef]
27. Mvondo, H.; den Brok, S.W.J.; Mvondo, O.J. Evidence for symmetric extension and exhumation of the Yaoundé nappe (Pan-African fold belt, Cameroun). *J. Afr. Earth Sci.* **2003**, *36*, 215–231. [CrossRef]
28. Mvondo, H.; Owona, S.; Mvondo, O.J.; Essono, J. Tectonic evolution of the Yaoundé segment of the Neoproterozoic central African Orogenic belt in southern Cameroon. *Can. J. Earth Sci.* **2007**, *44*, 433–444. [CrossRef]
29. Nédélec, A.; Macaudière, J.; Nzenti, J.P.; Barbey, P. Evolution structurale et métamorphique des schistes de Mbalmayo (Cameroun). Implications pour la structure de la zone mobile pan-africaine d'Afrique centrale, au contact du craton du Congo. *Comptes Rendus De L'académie Des Sci. Paris* **1986**, *303*, 75–80.
30. Toteu, S.F.; Deloule, E.; Penaye, J.; Tchamani, R. Preliminary U-Pb ionic microprobe data on zircons from Poli and Lom volcano-sedimentary basins (Cameroon): Evidence for a late—Mesoproterozoic to Early Neoproterozoic (1100-950 Ma) magmatic activity in the Central African Fold Belt. In Proceedings of the IGCP-470 2nd annual field conference, Garoua, Cameroun, 5–10 January 2004; p. 6.
31. Penaye, J.; Toteu, S.F.; Van Schumus, W.R.; Nzenti, J.P. U-Pb and Sm-Nd preliminary geochronologic data on the Yaoundé series Cameroon. Reinterpretation of the granulitic rocks as suture of a collision in the "Central African" Belt. *Comptes Rendus De L'académie Des Sci. Paris* **1993**, *317*, 789–794.
32. Ngako, V.; Jegouzo, P.; Nzenti, J.P. Le Cisaillement Centre Camerounais. Rôle structural et géodynamique dans l'orogenèse panafricaine. *C.R.A Sci. Paris.* **1991**, *313*, 457–463.
33. Bello, A.; Dawaï, D.; Antonio, P.Y.J.; Laurent, O.; Dopico, C.I.M.; Tchameni, R.; Vanderhaeghe, O. The deformed alkaline Balda granite (Northern Cameroon): A witness of back-arc basin in the northern part of Central African Orogenic Belt. *Precambr. Res.* **2024**, *410*, 107490. [CrossRef]
34. Delor, C.; Bernard, J.; Tucker, R.D.; Roig, J.-Y.; Bouyo Houketchang, M.; Couëffé, R.; Blein, O. *1:1 000 000-Scale Geological Map of Cameroon*, 2nd ed.; Ministry of Mines, Industry and Technological Development of Cameroon: Yaounde, Cameroon, 2021.
35. Winchester, J.A.; Floyd, P.A. Geochemical discrimination of different magma series and their differentiation products using immobile elements. *Chem. Geol.* **1977**, *20*, 325–343. [CrossRef]
36. Irvine, T.N.; Baragar, W.R.A. A guide to the chemical classification of the common volcanic rocks. *Can. J. Earth Sci.* **1971**, *8*, 523–548. [CrossRef]
37. Peccerillo, A.; Taylor, S.R. Geochemistry of Eocene calc-alkaline volcanic rocks from the Kastamonu area, northern Turkey. *Contrib. Mineral. Petrol.* **1976**, *58*, 63–81. [CrossRef]
38. Frost, B.R.; Barnes, C.G.; Collins, W.J.; Arculus, R.J.; Ellis, D.J.; Frost, C.D. A geochemical classification for granitic rocks. *J. Petrol.* **2001**, *42*, 2033–2048. [CrossRef]
39. Sun, S.-S.; McDonough, W. Chemical and isotopic systematics of oceanic basalts: Implications for mantle composition and processes. *Geol. Soc. Lond. Spec. Publ.* **1989**, *42*, 313–345. [CrossRef]
40. La Flèche, M.R.; Camiré, G.; Jenner, G.A. Geochemistry of post-Acadian, Carboniferous continental intraplaque basalts from the Maritimes Basin, Magdalen Islands, Québec, Canada. *Chem. Geol.* **1998**, *148*, 115–136. [CrossRef]
41. Thorarinsson, S.B.; Holm, P.M.; Duprat, H.I.; Tegner, C. Petrology and Sr–Nd–Pb isotope geochemistry of late cretaceous continental rift ignimbrites, Kap Washington peninsula, North Greenland. *J. Volcanol. Geotherm. Res.* **2012**, *219–220*, 63–86. [CrossRef]
42. Wood, D.A.; Gibson, I.L.; Thompson, R.N. Elemental mobility during zeolite facies metamorphism of the Tertiary basalts of eastern Iceland. *Contrib. Mineral. Petrol.* **1976**, *55*, 241–254. [CrossRef]
43. Thompson, G. Metamorphic and hydrothermal processes: Basalt-seawater interactions. In *Oceanic Basalts*; Floyd, P.A., Ed.; Springer: Berlin/Heidelberg, Germany, 1991; pp. 148–173.
44. Polat, A.; Hofmann, A.W. Alteration and geochemical patterns in the 3.7–3.8 Ga Isua greenstone belt, west Greenland. *Precambr. Res.* **2003**, *126*, 197–218. [CrossRef]
45. Floyd, P.A.; Winchester, J.A. Identification and discrimination of altered and metamorphosed volcanic rocks using immobile elements. *Chem. Geol.* **1978**, *21*, 291–306. [CrossRef]
46. Polat, A.; Hofmann, A.W.; Münker, C.; Regelous, M.; Appel, P.W.U. Contrasting geochemical patterns in the 3.7–3.8 Ga pillow basalts cores and rims, Isua greenstone belt, Southwest Greenland: Implications for post-magmatic alteration. *Geochim. Cosmochim. Acta* **2003**, *67*, 441–457. [CrossRef]

47. Xu, Y.; Chung, S.; Jahn, B.; Wu, G. Petrologic and geochemical constraints on the petrogenesis of Permian–Triassic Emeishan flood basalts in southwestern China. *Lithos* **2001**, *58*, 145–168. [CrossRef]
48. Frey, F.A.; Green, D.H.; Roy, S.D. Integrated models of basalt petrogenesis: A study of quartz tholeiites to olivine melilitites from Southeastern Australia utilizing geochemical and experimental petrological data. *J. Petrol.* **1978**, *19*, 463–513. [CrossRef]
49. Jung, S.; Masberg, P. Major- and trace-element systematics and isotope geochemistry of Cenozoic mafic volcanic rocks from the Vogelsberg (central Germany): Constraints on the origin of continental alkaline and tholeiitic basalts and their mantle sources. *J. Volcanol. Geotherm. Res.* **1998**, *86*, 151–177. [CrossRef]
50. Chazot, G.; Bertrand, H. Genesis of silicic magmas during tertiary continental rifting in Yemen. *Lithos* **1995**, *36*, 69–83. [CrossRef]
51. Kamgang, P.; Njonfang, E.; Nono, A.; Dedzo, M.G.; Tchoua, F.M. Petrogenesis of a silicic magma system: Geochemical evidence from Bamenda Mountains, NW Cameroon, Cameroon Volcanic Line. *J. Afr. Earth Sci.* **2010**, *58*, 285–304. [CrossRef]
52. Wendt, J.I.; Regelous, M.; Niu, Y.L.; Hekinian, R.; Collerson, K.D. Geochemistry of lavas from the Garrett Transform Fault: Insights into mantle heterogeneity beneath the eastern Pacific. *Earth Planet. Sci. Lett.* **1999**, *173*, 271–284. [CrossRef]
53. Alvaro, J.J.; Pouclet, A.; Ezzouhairic, H.; Soulaimanid, A.; Bouougrid, E.H.; Imaze, A.G.; Fekkakca, A. Early Neoproterozoic rift-related magmatism in the Anti-Atlas margin of the West African craton, Morocco. *Precambr. Res.* **2014**, *255*, 433–442. [CrossRef]
54. Davidson, J.; Turner, S.; Plank, T. Dy/Dy*: Variations arising from mantle source and petrogenetic processes. *J. Petrol.* **2013**, *54*, 525–537. [CrossRef]
55. Pearce, J.A.; Ernst, R.E.; Peate, D.; Rogers, C. LIP printing: Use of immobile element proxies to characterize large igneous provinces in the geologic record. *Lithos* **2021**, *392–393*, 106068. [CrossRef]
56. Asaah, A.N.E.; Yokoyama, T.; Aka, F.T.; Iwamori, H.; Kuritani, T.; Usui, T.; Gountié Dedzo, M.; Tamen, J.; Hasegawa, T.; Fozing, E.M.; et al. Major/trace elements and Sr–Nd–Pb isotope systematics of lavas from lakes Barombi Mbo and Barombi Koto in the Kumba graben, Cameroon Volcanic Line: Constraints on petrogenesis. *J. Afr. Earth Sci.* **2020**, *161*, 103675. [CrossRef]
57. Tchameni, R.; Sun, F.; Dawaï, D.; Danra, G.; Tékoum, L.; Nomo Negue, E.; Vanderhaeghe, O.; Nzolang, C.; Dagwaï, N. Zircon dating and mineralogy of the Mokong Pan-African magmatic epidote-bearing granite (North Cameroon). *Int. J. Earth Sci.* **2016**, *105*, 1811–1830. [CrossRef]
58. Green, N.L. Influence of slab thermal structure on basalt source regions and melting conditions: REE and HFSE constraints from the Garibaldi volcanic belt, northern Cascadia subduction system. *Lithos* **2006**, *87*, 23–49. [CrossRef]
59. Kwékam, M.; Affaton, P.; Bruguier, O.; Liégeois, J.-P.; Hartmann, G.; Njonfang, E. The Pan-African Kekem gabbro-norite (West-Cameroon), U–Pb zircon age, geochemistry and Sr–Nd isotopes: Geodynamical implication for the evolution of the Central African fold belt. *J. Afr. Earth Sci.* **2013**, *84*, 70–88. [CrossRef]
60. Khanna, T.C.; Sesha Saib, V.V. Petrogenesis of low-Ti and high-Ti basalt, adakite and rhyolite association in the Peddavuru greenstone belt, eastern Dharwar craton, India: A Neoarchean analogue of Phanerozoic-type back-arc magmatism. *Geochemistry* **2020**, *80*, 125606. [CrossRef]
61. Gorton, M.P.; Schandl, E.S. From continents to Island arcs: A geochemical index of tectonic setting for arc-related and within-plate felsic to intermediate volcanic rocks. *Can. Mineral.* **2000**, *38*, 1065–1073. [CrossRef]
62. Shaw, D.M. Trace element fractionation during anatexis. *Geochim. Cosmochim. Acta* **1970**, *34*, 237–248. [CrossRef]
63. Jung, C.; Jung, S.; Hoffer, E.; Berndt, J. Petrogenesis of tertiary mafic alkaline magmas in the hocheifel, Germany. *J. Petrol.* **2006**, *47*, 1637–1671. [CrossRef]
64. Wang, K.; Plank, T.; Walker, J.D.; Smith, E.I. A mantle melting profile across the Basin and Range, SW USA. *J. Geophys. Res.* **2002**, *107*, ECV 5-1–ECV 5-21. [CrossRef]
65. Pearce, J.A. Geochemical Fingerprinting of Oceanic Basalts with Applications to Ophiolite Classification and the Search for Archean Oceanic Crust. *Lithos* **2008**, *100*, 14–48. [CrossRef]
66. Gurenko, A.; Hoernle, K.; Hauff, F.; Schmincke, H.; Han, D.; Miura, Y.; Kaneoka, I. Major, trace element and Nd-Sr-Pb-O-He- Ar isotope signatures of shield stage lavas from the central and western Canary Islands: Insights into mantle and crustal processes. *Chem. Geol.* **2006**, *233*, 75–112. [CrossRef]
67. Innocenti, F.; Agostini, S.; Di Vincenzo, G.; Doglioni, C.; Manetti, P.; Savaşçin, M.Y.; Tonarini, S. Neogene and quaternary volcanism in western anatolia: Magma sources and geodynamic evolution. *Mar. Geol. Miocene Recent. Tecton. Evol. East. Mediterr.* **2005**, *221*, 397–421. [CrossRef]
68. Barbarin, B. A review of the relationships between granitoid types, their origins and their geodynamic environments. *Lithos* **1999**, *46*, 605–626. [CrossRef]
69. Pearce, J.A.; Harris, N.B.W.; Tindle, A.G. Trace element discrimination diagrams for the tectonic interpretation of granitic rocks. *J. Petrol.* **1984**, *25*, 956–983. [CrossRef]
70. Cabanis, B.; Lecolle, M. Le diagramme La/10-Y/15-Nb/8: Un outil pour la discrimination des séries volcaniques et la mise en évidence des processus de mélange et/ou de contamination crustale. *Comptes Rendus de l'Academie des Sciences. Serie 2* **1989**, *309*, 2023–2029.
71. Wood, D.A. The application of a Th-Hf-Ta diagram to problems of tectonomagmatic classification and to establishing the nature of crustal contamination of basaltic lavas of the British Tertiary Volcanic Province. *Earth Planet. Sci. Let.* **1980**, *50*, 11–30. [CrossRef]
72. Müller, D.; Groves, D.I. Definitions and nomenclature. Potassic Igneous Rocks and Associated Gold-Copper Mineralization. In *Lecture Notes in Earth Sciences*; Müller, D., Groves, D.I., Eds.; Springer: Berlin/Heidelberg, Germany, 1995; pp. 3–10.

73. Defant, M.; Drummond, M.S. Derivation of some modern arc magmas by melting of young subducted lithosphere. *Nature* **1990**, *347*, 662–665. [CrossRef]
74. McDonough, W.F.; Sun, S.S. The composition of the Earth. *Chem. Geol.* **1995**, *120*, 223–253. [CrossRef]